31st Congress of the International Council of the Aeronautical Sciences
Belo Horizonte, Brazil; September 09-14, 2018

PROPELLER OPTIMISATION FOR AN ELECTRICALLY-POWERED TACTICAL UAS

Rens MacNeill* **and Dries Verstraete***
***The University of Sydney, New South Wales, 2006, Australia**

Keywords: *Propeller, Electric-Motor, Regression, Optimisation, Pareto-optimality*

Abstract

Small, electrically powered unmanned aerial systems are increasingly used for tactical surveillance and reconnaissance. To increase the endurance of small tactical UAS, significant research effort has been concentrated on battery technology. However off-the-shelf propellers are commonly used. This paper presents propeller optimisation for an electrically-powered tactical UAS. A multidisciplinary design tool is developed, including a regression-corrected electric motor analysis method. The maximisation of powertrain efficiency is investigated using multi-objective optimisation, allowing the coupling of propeller and motor efficiencies to be seen. Both single flight-condition and multiple flight-condition optimisation are investigated. In addition, Pareto optimality between powertrain efficiency and other design goals is investigated and presented.

1 Introduction

Unmanned aerial systems (UAS) are currently operated predominantly for the purposes of reconnaissance and surveillance [1]. Meanwhile the development of smaller tactical UAS making use of electric powertrains has rapidly increased in recent years [1]. With battery technology having improved markedly in the past two decades [1], this increase can be directly attributed to the increased relative energy density, high efficiency, relative simplicity and low noise signature of brushless direct-current (DC) electric motor systems [2]. The endurance of an unmanned vehicle is largely dictated by the performance and efficiency of the propeller and the powertrain, and recent research is focused on technology to effect increased efficiency in the powertrains of unmanned vehicles [1, 3–9]. However it is still common practice to use commercial off-the-shelf, fixed-pitch propellers with these powertrains even for the most sophisticated tactical UAVs [10].

Propeller design for small UAS platforms has often exclusively been concerned with aerodynamic optimisation with the goal of maximising propeller efficiency [11, 12]. When using a serial design procedure such as this, the propeller is subject to other constraints only following the completion of aerodynamic design, which then provides no guarantee of overall optimality. Multidisciplinary optimisation on the other hand, allows the design goals and constraints of multiple disciplines to be considered simultaneously during the optimisation process [13]. Gur and Rosen [14, 15] considered structural and acoustic constraints alongside aerodynamic performance in a notable application of multidisciplinary optimisation to propeller design for a small electrically-powered UAS.

The design of propellers for small UAS often considers the design of the propeller independent of the vehicle powertrain [16–18]. However this can cause noteworthy reductions in vehicle performance if the propeller and powertrain are not precisely matched. The efficiency of the propulsion system is, after all, the product of the propulsion system and propeller efficiencies [19]. With

this in mind, optimal propeller design must consider not just the aerodynamic performance of the propeller and the satisfaction of structural and other constraints, but the operating points of the powertrain to which the propeller is coupled, at each design point [15, 19].

Propeller design and optimisation specifically for electrically powered unmanned aerial systems has been the focus of increased research in conjunction with the increased popularity of electric UAS [14, 15, 20, 21]. Meanwhile the design and optimisation of propellers for electric motors coupled to internal combustion engines has also been investigated [22–24]. However the design of a propeller specifically for small electric UAS in combination with the rest of the powertrain often requires a motor to be chosen a priori such that its performance can be characterised. In this paper, a regression analysis is conducted using a large number of electric motors, allowing the derivation of a number of expressions which characterise motor performance. In this way, a notional electric motor can be used during the design process of the propeller, and a suitable combination of both propeller and powertrain can be quickly and easily established by the designer.

To effectively increase vehicle endurance and range, efficient operation across the design mission is required, which means multiple operating conditions must be considered during propeller design [15, 21, 25]. In this paper, the NSGA-II algorithm is used to conduct multi-objective optimisation [26]. Optimisation of the propulsion system to maximise endurance, range, climb-rate and maximum flight-velocity are explored, and Pareto-optimality between the combinations of these design goals are presented.

2 Analysis Models

2.1 Electric Motor Model

In this paper, an empirically-corrected first order model is used to analyse brushless DC electric motor performance. The model, derived from first principles by Drela [27] details the equivalent internal circuit model of a DC electric motor as that found in Fig 1.

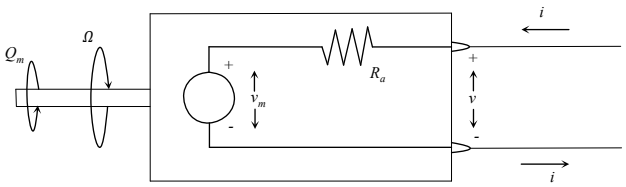

Fig. 1 Equivalent circuit for a DC electric motor (adapted from Drela [27])

As described by Drela [27], the resistance of the motor $\mathcal{R}$ is assumed to be constant and the shaft torque Q_m is assumed to be proportional to the current i through the torque constant K_Q. The friction related losses in the motor can be accounted for using a no-load current i_0.

$$Q_m(i) = (i - i_0)K_Q \tag{1}$$

The internal voltage (back-EMF) of the motor v_m is assumed to be proportional to the rotational rate Ω through the motor speed constant K_V.

$$v_m(\Omega) = \Omega / K_V \tag{2}$$

The motor terminal voltage can then be obtained by adding the voltage drop due to motor resistance

$$v(i,\Omega) = v_m(\Omega) + i\mathcal{R} = \Omega/K_V + i\mathcal{R} \tag{3}$$

Using this model, the performance of any DC brushless motor can be simulated if the first order motor constants $K_V, K_Q, \mathcal{R}$ and i_0 are known. In this paper, each of the constants are obtained using a regression-based approach of 1743 DC electric motors, the methodology for which is detailed in the work by Verstraete et al. [28]. The results of the current regression analysis are described in sections 2.1.1 and 2.1.2.

Once the motor constants are known, the equations describing the motor model can be rearranged to give current, torque, power and motor efficiency, with each parameter a function of motor rotational speed and terminal voltage. The current is obtained from Eq 3.

$$i(\Omega, v) = \left(v - \frac{\Omega}{K_V}\right)\frac{1}{\mathcal{R}} \tag{4}$$

The functions describing the other motor variables follow. It should be noted here that the torque constant K_Q is set equal to the motor speed constant K_V following the method presented by Drela [27], which then gives:

$$\begin{aligned} Q_m(\Omega, v) &= \left[i(\Omega, v) - i_0\right] \frac{1}{K_V} \\ &= \left[\left(v - \frac{\Omega}{K_V}\right)\frac{1}{\mathcal{R}} - i_0\right]\frac{1}{K_V} \\ P_{shaft}(\Omega, v) &= Q_m \Omega \\ \eta_m(\Omega, v) &= \frac{P_{shaft}}{iv} \\ &= \left(1 - \frac{i}{i_0}\right)\frac{1}{1 + i\mathcal{R}K_V/\Omega} \end{aligned} \tag{5}$$

2.1.1 *Motor Mass and Dimensions*

Motor mass and dimensions are related to the motor power output [15, 29], and motor mass is thus expected to increase with continuous motor power (Fig. 2). The correlation between motor mass and continuous power is given by:

$$m_M = 8.14 \times 10^{-4} P_{cont}^{0.8092} \tag{6}$$

where P_{cont} is the motor continuous power [W] and m_M is the motor mass [kg]. For the considered motors, the power-to-mass ratio varies between approximately

$$2.0\,\mathrm{kW/kg} < \frac{P_{cont}}{m_M} < 12.5\,\mathrm{kW/kg}$$

These limits are indicated by the black lines on Fig. 2. While this presents a relatively large variation in power-to-mass, this spread partially stems from the different speed constants of the motors. The remainder of the variation most likely arises from the use of different magnetic materials, design concepts, or manufacturing methods [15]. For motors with a continuous power rating above 30 kW a typical value of 6.0 kW/kg should be used rather than extrapolating the current trend line. This value is consistent with reported specific powers for state-of-the-art large electric motors for aeronautical and automotive applications [30, 31]. However, the derived power law incorporates the comparatively larger effects of secondary masses like connectors for smaller motors and is more appropriate for small UAVs.

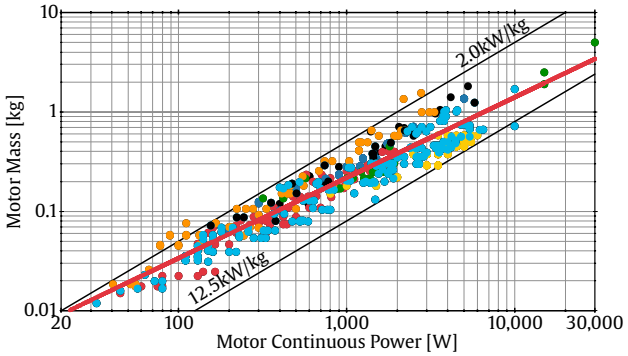

Fig. 2 Motor mass as function of motor continuous power output with colours indicating different manufacturers. Only the largest subsets are coloured.

Eq. (6) allows the motor mass to be derived from the required continuous power of the motor. However, during high-power demand phases like climb and take-off motors are often used at a higher power rating for a short period of time. The ratio between peak power and continuous power was therefore analysed for all motors in the database. Large variations exist in the published values for this ratio. Values ranging from 10% additional power to 100% additional power are reported for the considered brushless DC motors. For a preliminary study the average value of the entire motor dataset is recommended:

$$\frac{P_{peak}}{P_{cont}} = 1.4 \tag{7}$$

The motor diameter D and motor length L should, according to the cube-square law [32–34], scale with the motor mass to the power 1/3. The following correlation was therefore used to determine motor dimensions:

$$D_M = C_{DM} m_M^{1/3} \tag{8}$$

$$L_M = C_{LM} m_M^{1/3} \tag{9}$$

where C_{DM} and C_{LM} are proportionality constants that are derived through a non-linear least-squares regression analysis. Values of 68.81

mm/kg$^{1/3}$ and 80.68 mm/kg$^{1/3}$ were found for the proportionality constants for diameter and length. While those values give reasonable results for the current database, a fairly large variation in motor dimensions exist:

$$45\,\text{mm/kg}^{1/3} < C_{DM} < 100\,\text{mm/kg}^{1/3}$$
$$60\,\text{mm/kg}^{1/3} < C_{LM} < 120\,\text{mm/kg}^{1/3}$$

2.1.2 *Motor Performance Constants*

Motor performance is calculated from three (so-called) motor constants: the motor speed constant K_V, the motor resistance $\mathcal{R}$, and the motor zero-load current i_0. Statistical scaling laws for those 3 constants are derived next.

The motor speed constant K_V is directly related to the motor size. The torque constant (the inverse of the speed constant) depends on the motor flux linkage and the magnetic circuit [15]: the larger the motor, the larger the flux linkage and torque constant. As the motor becomes heavier and more powerful, the speed constant thus decreases. Fig. 3 presents the normalised motor speed constant versus motor mass for the entire database, where the normalised speed constant is given as K_V/m_M.

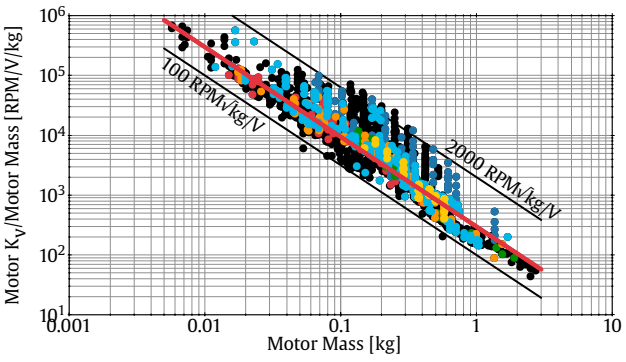

Fig. 3 Motor speed constant as function of motor mass with colours indicating different manufacturers. Only the largest subsets are coloured.

The non-linear regression analysis shows that the speed constant is inversely proportional to the square root of the motor mass:

$$K_V = \frac{C_{K_V}}{\sqrt{m_M}} \tag{10}$$

where C_{K_V} is a speed-constant parameter. For the majority of the database this parameter falls between the following values (black lines on Fig. 3):

$$100\,\text{RPM}\sqrt{\text{kg}}/V < C_{K_V} < 2000\,\text{RPM}\sqrt{\text{kg}}/V$$

This range indicates that a considerable variation exists in the speed constant. This is expected as motors of a given power rating (and mass) are often designed with a different K_V to allow a range of propeller sizes to be selected. Lower K_V motors provide more torque so that they can turn larger (more efficient) propellers. Similar motors with a different K_V rating are noticeable on Fig. 3 as a vertical cluster of points.

A typical value of:

$$C_{K_V} = 298.3\,\text{RPM}\sqrt{\text{kg}}/\text{V} \tag{11}$$

is proposed, as determined by the regression analysis. This value is indicated by the red line on Fig. 3. While seemingly on the low end of the data range, many data points are grouped towards this end of the spectrum and the red line on Fig. 3 denotes the value of C_{K_V} that produces the best match with the dataset.

Rather than fitting motor resistance as a standalone parameter, the internal resistance is grouped with the motor speed constant to obtain a smaller variation in values (Fig. 4). The trend of a reduction in $\mathcal{R}\cdot K_V$ with motor mass is clear, and the following relation is obtained from the regression analysis:

$$\frac{\mathcal{R}\cdot K_V}{m_M} = 3.262 m_M^{-2.2591} \tag{12}$$

The bounds that encompass the majority of the dataset are also given on Fig. 4. They present values for the proportionality constant that range between:

$$1\,\Omega\text{kg}^{1.2591}\text{RPM/V} < C_{\mathcal{R}} < 10\,\Omega\text{kg}^{1.2591}\text{RPM/V}$$

The goodness-of-fit of this correlation is shown by the R^2-value of 0.9991, and the relatively small spread on the proportionality constant. While the range of the proportionality constant is still considerable, rearranging and combining parameters has resulted in a much smaller variation than reported previously [15].

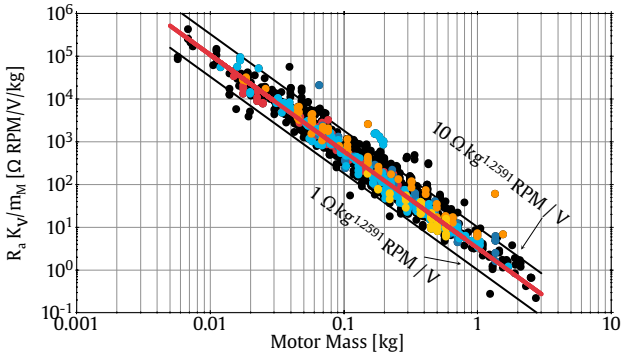

Fig. 4 Motor resistance as function of motor mass with colours indicating different manufacturers. Only the largest subsets are coloured.

Finally, the zero-load current is obtained as function of motor mass. To account for the large variation in speed constant values, the zero-load current is normalised by the motor K_V-value and its mass. This results in the following correlation (Fig. 5):

$$\frac{i_0 \cdot m_M}{K_V} = 9.104 \times 10^{-3} m_M^{1.9778} \qquad (13)$$

This correlation has an R^2-value of 0.9971. The range for the proportionality constant indicated on Fig. 5 is

$$0.003\,\mathrm{AV/RPM/kg} < C_{i_0} < 0.03\,\mathrm{AV/RPM/kg}$$

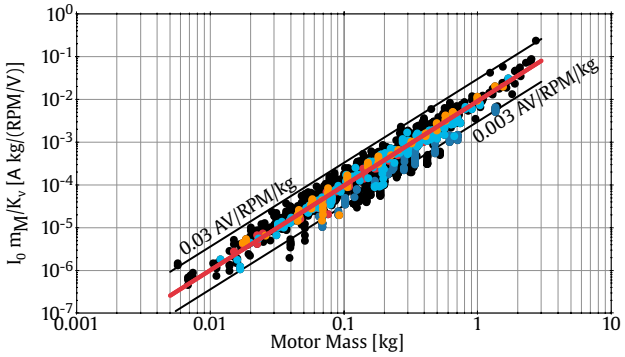

Fig. 5 Motor zero-load current as function of motor mass with colours indicating different manufacturers. Only the largest subsets are coloured.

2.2 Aerodynamic Model

In this paper, the aerodynamic forces and moments produced by each propeller blade are calculated using a blade element momentum-theory (BEMT) method, which enables thrust and torque values to be computed for each candidate propeller. The aerodynamic loads experienced by the propeller are then passed to the structural solver to compute the stress levels faced by each propeller blade. The accuracy of the model is obviously paramount to valid propeller optimisation. Blade element momentum-theory is the most commonly used tool for propeller design, in particular in the context of optimisation, largely due to its computational efficiency [11, 15, 35]. BEMT methods offer relatively good accuracy, provided the blade sections are not stalled and the flow is at a relatively high Reynolds number [12]. Outside of these conditions, the ability of BEMT methods to accurately predict propeller performance degrades rapidly. The aerodynamic model used in this paper is a BEMT method extended to account for low Reynolds number and rotational effects, while also including high angle of attack aerodynamics. For a detailed description and validation of the method, the reader is directed to references [12, 19, 36].

2.3 Structural Model

To ensure each propeller blade can withstand the stresses resulting from both aerodynamic and inertial loadings, structural analysis is required during optimisation. To achieve the required accuracy and computational efficiency, a three dimensional Euler-Bernoulli beam theory finite element model has been implemented [37, 38], similar to the method used by the authors in previous work [19, 36].

Briefly, the finite element model discretises the elastic axis of the propeller blade into a number of spanwise elements. The cross-sectional structural properties are assumed to be uniform across each element and are equivalent to the properties of the propeller blade cross section at

that radial position. The stiffness matrices, loading vectors and displacement vectors of each element are formulated and assembled into matrices characterising the entire propeller blade. The applied aerodynamic and inertial loads combined with the stiffness of the blade then determine the deflection of each point along the elastic axis. This allows the residual forces applied along the elastic axis to be found, which in turn allows calculation of stress values along the propeller blade.

3 Optimisation Problem

Propeller optimisation presents a nonlinear optimisation problem subject to certain constraints. In general, optimisation is concerned with the minimisation of a function $f_0(x)$, where x is a vector of design variables. The function $f(x)$, known as the *cost function* or *objective function*, is used to express how optimal each design candidate is. The optimisation problem is subject to both inequality $f_i(x)$ and equality $h_i(x)$ constraints. Borrowing terminology from Boyd and Vandenberghe [39], we use the notation

$$\begin{aligned} \underset{x}{\text{minimise}} \quad & f_0(x) \\ \text{subject to} \quad & f_i(x) \leq 0,\ i = 1,\dots,m \\ & h_i(x) = 0,\ i = 1,\dots,p \end{aligned} \tag{14}$$

to describe the problem of finding a vector x that minimises $f_0(x)$ among all x that satisfy the conditions $f_i(x) \leq 0$, $i = 1,\dots,m$, and $h_i(x) = 0$, $i = 1,\dots,p$. The constrained optimisation problem given by Eq. (14) can be modified to its equivalent unconstrained form using a penalty method, similar to the use of Lagrangian multipliers [39]. In this way, the optimisation problem then becomes

$$\begin{aligned} \text{minimise} \quad g(x,\lambda,\nu) = & f_0(x) \\ & + \sum_{i=1}^{m} \lambda_i \tilde{f}\big(f_i(x)\big) \\ & + \sum_{i=1}^{p} \nu_i \tilde{h}\big(h_i(x)\big) \end{aligned} \tag{15}$$

The shape of the penalty functions λ and ν has a significant influence on the solution of the penalty function optimisation problem [39]. In this paper, quadratic penalty functions are used, which are of the following form

$$\begin{aligned} \tilde{h}\big(h_i(x)\big) &= h_i^2(x) \\ \tilde{f}\big(f_i(x)\big) &= \begin{cases} 0 & f_i(x) \leq 0 \\ f_i^2(x) & f_i(x) > 0 \end{cases} \end{aligned} \tag{16}$$

In this paper, a number of competing design goals are optimised at one time using so-called 'multi-objective optimisation'. Propeller optimisation for maximum aircraft endurance, range, climb-rate and flight-velocity have been examined, as well as Pareto-optimality between the combinations of these competing design considerations. Pareto-optimality between competing design goals has been implemented using the NSGA-II algorithm [26]. NSGA-II is a genetic algorithm capable of multi-objective optimisation. When considering multi-objective optimisation, the algorithm produces a Pareto front between two or more competing design goals such that the 'optimal' design can be determined depending on the priorities of the case in question.

3.1 Optimisation Process

The population size and maximum number of generations provided to the NSGA-II algorithm in the study are 250 and 75 respectively, of which both parameters have been sized to provide sufficient exploration of the design space along with reasonable convergence characteristics and computational demands.

The initial population was generated using latin hypercube sampling [40, 41]. A known feasible solution is inserted into the initial population to ensure that the genetic algorithm is seeded with at least one feasible solution at the beginning of each generation.

For both the maximum-endurance and maximum-range flight conditions, the thrust produced by the propeller must be equal to the drag of the aircraft. As the geometry of each design-candidate propeller is fixed, the target variable for this constraint is the rotational speed of the propeller. The rotational speed of the propeller is found and the constraint satisfied using

a nonlinear root-finder. Meanwhile in the case of climb-rate or flight-velocity maximisation, the geometry is fixed and the rotational speed is the design variable that must be varied. For both climb-rate and flight-velocity maximisation, the fast and efficient Nelder-Mead simplex method is used.

Once the aerodynamic performance of the propeller has been obtained at any flight condition, structural constraints are applied. If the propeller fails structurally, the design is rejected by applying severe penalties and bypassing any further objective function calculations. If satisfactory structural performance is obtained, the point at which the propeller and powertrain are matched is examined. If the point at which the two are matched exists outside the bounds of the motor map (with examples seen in Fig. 7), a penalty function is applied. This holds for both rotational speeds and torque values that lie outside the viable region of the motor map.

Given that the propeller and motor are matched at a feasible motor operating point, the operating conditions of the motor must be found, which then dictates an efficiency level at which the motor (and the rest of the powertrain) will be operating for the current combination of flight condition and propeller.

3.2 Design Variables

The design variables in this study are firstly those which can be considered general propeller design variables. These are comprised of: the number of propeller blades n_b; the propeller radius R; the material from which the propeller is constructed. In this paper, the propeller radius is allowed to vary continuously, however the blade number is selected by the designer.

The second set of design variables relate to the propeller planform, namely the chord c and twist β distributions of the propeller. In this paper, both the chord and the twist angle have been discretised using quartic polynomials along the blade span, to ensure continuity across the blade, the lack of which was shown to be problematic by Gur and Rosen [11]. Five control points are used along the blade span, such that a unique fourth-order polynomial may be fitted through them. Mathematically this is represented as

$$c(r) = c_0 + c_1 r + c_2 r^2 + c_3 r^3 + c_4 r^4 \tag{17}$$

$$\beta(r) = \beta_0 + \beta_1 r + \beta_2 r^2 + \beta_3 r^3 + \beta_4 r^4 \tag{18}$$

In this analysis, the control points r_{cp} are located along the blade radius according to

$$\frac{r_{cp}}{R} = \begin{bmatrix} 0.15 & 0.30 & 0.50 & 0.80 & 1.00 \end{bmatrix} \tag{19}$$

The sectional design variables in this report consist of airfoil selection from a pool of possible airfoils, thereby making the sectional design variables integer design variables. The group of airfoils provided to the optimiser in this study are those in the NACA 43XX, 44XX and 45XX families of thickness 6%, 9%, 12%, 15%, 18% or 21%. The choice of airfoil is passed to the optimisation as an integer variable, representing a discrete choice between possible airfoils.

The optimisation domain or search space is a p-dimensional domain where p is the number of design variables. In this paper, the search space is of dimension $p = 26$, with one design variable setting the propeller diameter, 5 chord control point design variables, 5 twist control point design variables, and 15 radial stations at which the airfoil is varied. The range of each dimension is set by upper and lower bounds of that specific variable.

In this study, the number of propeller blades has been held constant at 2 for each case, while the construction material of the propeller is fixed as 30% glass-plastic reinforced composite, with a tensile yield stress $\sigma_{t_y} = 90MPa$ [42]. The propeller diameter was allowed to vary freely between a lower and upper bounds of 8 and 20 inches respectively (203.2mm & 508.0mm).

The lower and upper bounds of the propeller blade chord at each of the polynomial control points are given by:

$$\begin{aligned} c_{control_{min}}[mm] &= [10, 10, 10, 10, 5] \\ c_{control_{max}}[mm] &= [50, 100, 100, 100, 10] \end{aligned} \tag{20}$$

Meanwhile the upper and lower bounds of the twist control point values at each control point location are $7\pi/16$ and $-\pi/6$ radians respectively. Both the chord and twist bounds have been set by considering the characteristics of propellers of similar size to those considered in this paper [12, 36].

4 Propeller Optimisation for a Small Hybrid Electric Fuel-Cell UAS

A Grob G109 scale high aspect ratio glider, is used in this paper as the test bed for propeller optimisation. This aircraft was chosen as the test airframe for hybrid fuel-cell flight testing by Gong and Verstraete [8] due to its highly efficient nature, and is shown during one of these flight tests in Fig. 6.

Fig. 6 Grob G109 Scale Aircraft

The characteristics of the aircraft are summarised in Table 1.

Table 1 Characteristics of Grob G109 Scale Glider [8]

Parameter	Units	Value
Aircraft takeoff mass $m_{aircraft}$	$[kg]$	5.32
Wing area S	$[m^2]$	0.568
Wing span b	$[m]$	2.77
Oswald efficiency e	$[-]$	0.9
Zero-angle lift coefficient C_{L_0}	$[-]$	0.28
Zero-lift drag coefficient C_{D_0}	$[-]$	0.0325

The Grob G109 testbed has a single nose-mounted propeller driven by an electric motor. In this paper, a suitably-sized notional electric motor has been used as the basis for coupled propeller/powertrain optimisation. The parameters characterising the performance of the notional motor were calculated using the nominal proportionality constants presented in sections 2.1.1 and 2.1.2, with the exception of the speed constant proportionality constant C_{K_V} where a value of $C_{K_V} = 200.0\,\mathrm{RPM}\sqrt{\mathrm{kg}}/\mathrm{V}$ was used to match the Rimfire 0.55 480kV motor motor used during flight tests more closely [9]. The resulting motor parameters are summarised in Table 2.

Table 2 Notional Motor Performance Parameters

Parameter	Units	Value
Continuous power P_{cont}	[Watts]	280
Motor mass m_M	[kg]	0.140
Motor diameter D_M	[mm]	36.0
Motor length L_M	[mm]	42.0
Speed constant K_V	[RPM/volt]	473
Motor resistance $\mathcal{R}$	[Ohms]	0.0845
Zero-load current i_0	[Amps]	0.6150

Both the torque and power maps of the motor generated using the electric motor model set out in this paper along with the derived constants are shown in Fig. 7. These maps compare favourably to experimentally-derived maps generated using the Rimfire 0.55 480kV motor [9], showing the validity of the electric motor regression analysis developed in this paper.

The lift coefficient of the aircraft can be computed at each flight condition, and the corresponding drag coefficient is found using a typical aircraft drag polar as given in Eq. (21).

$$C_D = C_{D_0} + \frac{1}{\pi \cdot AR \cdot e}(C_L - C_{L_0})^2 \qquad (21)$$

Two operating altitudes are used in this analysis, a nominal cruise altitude at which both endurance and range are optimised, and a lower altitude at which climb-rate optimisation will be investigated. The optimisation of maximum flight speed is also conducted at the nominal cruise altitude. The climb speed is set at 1.25 times the

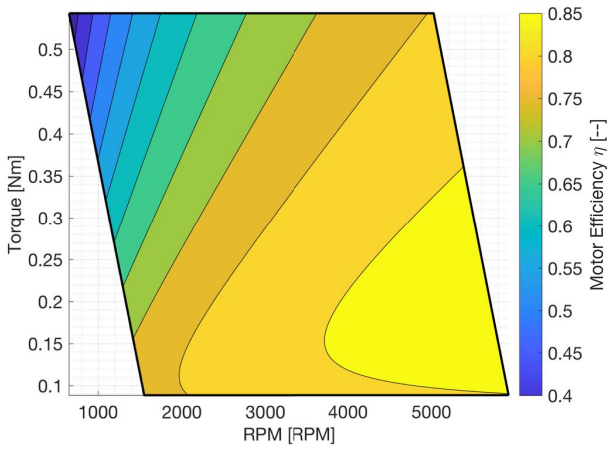

(a) Torque

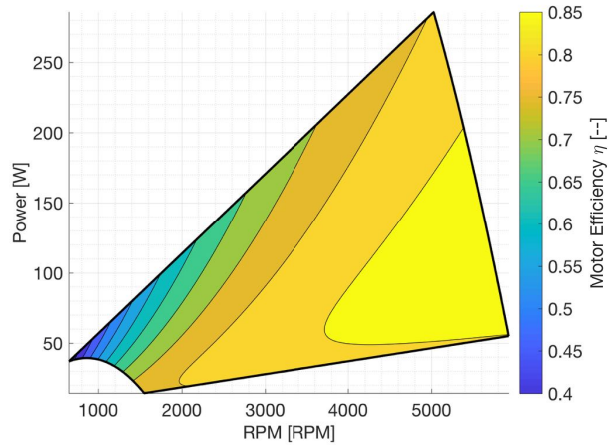

(b) Power

Fig. 7 Motor torque and power maps

stall speed. The operating conditions used in this study are summarised in Table 3.

4.1 Single Flight-Condition Design

Two of the more obvious cases for propeller optimisation for small tactical UAS are the maximisation of both vehicle endurance and range. Both endurance and range are maximised when the energy usage is minimised, i.e. when the powertrain efficiency is maximised.

The efficiency of the powertrain is given by the product of the efficiencies of each of its components, of which the motor and the propeller are often the most influential. With the maximisation of overall efficiency the primary goal, Pareto fronts of propeller efficiency $\eta_{propeller}$ and motor efficiency η_{motor} are presented. Contours of combined efficiency are overlaid to highlight the highest overall efficiency between motor operating point and candidate propeller design.

To aid in the interpretation of results, points on each Pareto front have been coloured according to the twist angle at 80% of the blade radius. In a similar way, the size of each point corresponds to the propeller diameter.

4.1.1 Endurance

Fig. 8 presents a Pareto front of propeller and motor efficiencies for the maximisation of aircraft endurance. The propellers of lower diameter with relatively higher twist occupying the upper left corner of the Pareto front are the designs that achieve higher motor efficiencies. This is because in general, a lower diameter propeller must be spun faster to produce the same thrust, even when accounting for the increased twist. Their relatively higher operating RPM values result in the motor operating in higher efficiency regions of its operating map, which can be seen in Fig. 7. The highest combined efficiency powertrain solution has an overall efficiency of 67.97%, achieved with propeller and motor efficiencies of 79.8% and 85.2% respectively as shown in Table 4.

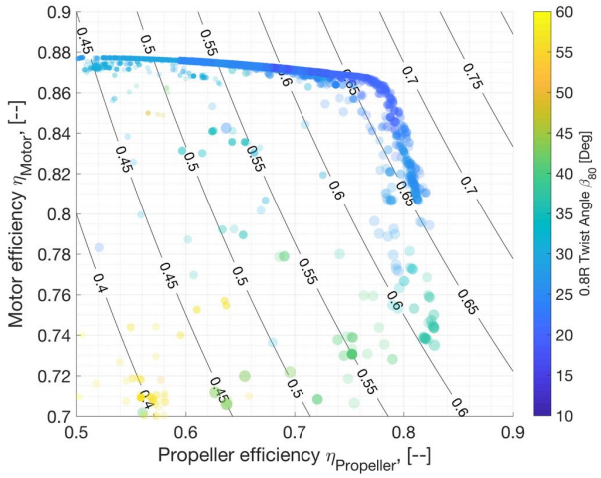

Fig. 8 Propeller efficiency vs motor efficiency at maximum endurance flight condition

Table 4 depicts the parameters of optimal propellers designed for endurance and range

Table 3 Mission operating conditions

		Operating condition		
Parameter	Units	Endurance	Range	Climb
Altitude h	$[m]$	500	500	50
Density ratio σ	$[-]$	0.953	0.953	0.995
V_{flight}	$[m/s]$	12.32	16.21	13.02
Drag D	$[N]$	3.03	3.48	3.05

where each 'optimal' propeller has been extracted using the simple criterion of maximum combined powertrain efficiency.

4.1.2 Range

Many of the same trends observed in Fig. 8 are also present in the Pareto fronts obtained when examining propeller optimisation for maximum range, as shown in Fig. 9. The highest combined efficiency for a propeller optimised for aircraft range is just over 70% through a propeller efficiency of 82.7% and a motor efficiency very similar to the endurance case of 85.5%.

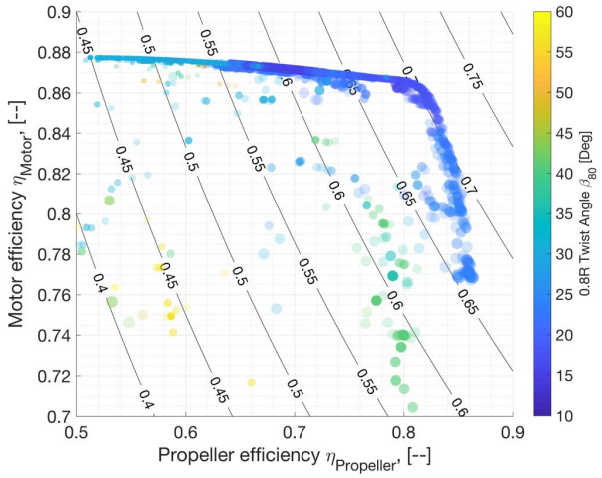

Fig. 9 Propeller efficiency vs motor efficiency at maximum range flight condition

A comparison between propellers optimised for maximum aircraft endurance and those optimised for maximum aircraft range shows that the range optimised propellers produce propeller and overall efficiency values on the order of 2.5% higher than the endurance-optimised propellers. This also results in higher overall efficiencies as shown by the position of the Pareto front relative to the overlaid contours. However, as the velocity of the aircraft is higher at its optimal range operating point than its optimal endurance operating point, the higher efficiency will not necessarily correspond to lower energy usage than at the endurance operating point. This does suggest however that the motor is perhaps slightly oversized if endurance maximisation is the goal.

Fig. 10 shows the difference in blade geometry for an optimal propeller designed for maximum aircraft endurance when compared to an optimal propeller designed for maximum aircraft range. Given the close proximity of the maximum-endurance and range velocities for the testbed aircraft, it comes as no surprise that the optimal propellers for each flight condition have very similar geometries. The endurance-optimised propeller does show a higher chord from around $0.4r/R$ outboard, as well as marginally higher twist values towards the root. These factors, combined with the slightly higher propeller diameter of the endurance-optimised propeller allow it to satisfy the thrust requirements while rotating 1000rpm slower than its range-optimised counterpart at their respective design points.

4.2 Multiple Flight-Condition Design

Some compromise between different aspects of vehicle performance is essential for practical propeller optimisation. The maximisation of powertrain efficiency then becomes a multi-objective optimisation problem, and Pareto optimisation is ideally suited. In this section, the results of various multi-objective optimisation cases are presented. First, a multi-objective optimisation be-

Table 4 Optimal propellers at differing flight conditions

Parameter	Units	Endurance	Range
Diameter D	$[in]$	11.97	11.78
RPM	$[RPM]$	3000	4000
Thrust T	$[N]$	3.08	3.48
Power P	$[W]$	46.8	68.3
Propeller efficiency $\eta_{propeller}$	$[-]$	0.798	0.827
Motor efficiency η_{motor}	$[-]$	0.852	0.855
Overall efficiency $\eta_{overall}$	$[-]$	0.680	0.707

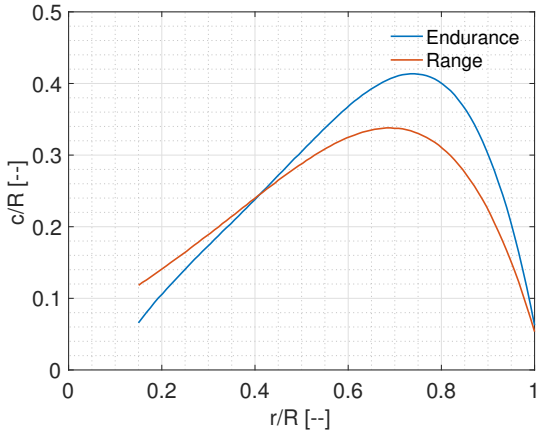

(a) Normalised chord distribution

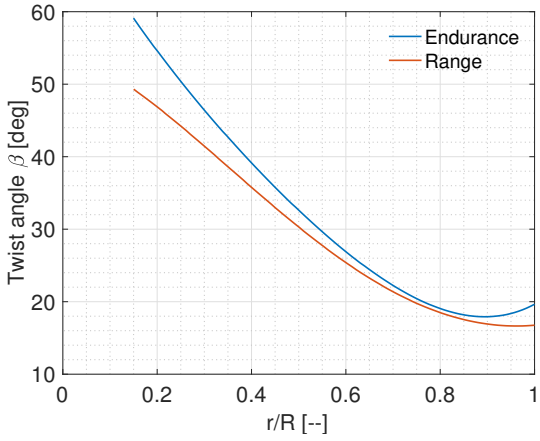

(b) Twist distribution

Fig. 10 Optimal propeller geometry for endurance & range

tween aircraft endurance and range is shown, followed by multi-objective optimisation cases of combined powertrain efficiency and either maximum climb-rate or maximum flight-velocity.

4.2.1 Endurance vs Range

Again, with the close proximity ($<$ 4m/s) of the endurance and range flight velocities, it is expected that a propeller optimised for one condition should operate fairly efficiently at the other, and vice versa. The minimal spread and linear nature of the Pareto front shown in Fig. 11 clearly shows this expected result, as optimal propellers designed for either the maximum endurance or maximum range operate with relatively high efficiency at both flight conditions. This figure also shows the previously identified slightly higher overall efficiency at the maximum range operating condition.

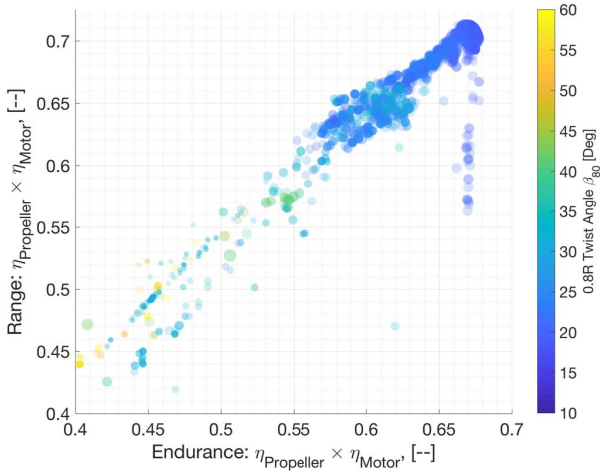

Fig. 11 Optimal propeller design for endurance vs range

4.2.2 Climb Rate

While high efficiency during loiter and cruise is desired, a high climb-rate is also required for a

small tactical UAS, allowing the operating altitude to be reached as quickly as possible. This section presents the Pareto-optimality between the combined motor and propeller efficiency at the endurance and range conditions with maximum aircraft climb-rate at the nominal climb speed. Examining Fig. 12, the expected result of relatively low-pitch propellers when designing for maximum climb-rate is clearly shown by the blue colour of the active Pareto front.

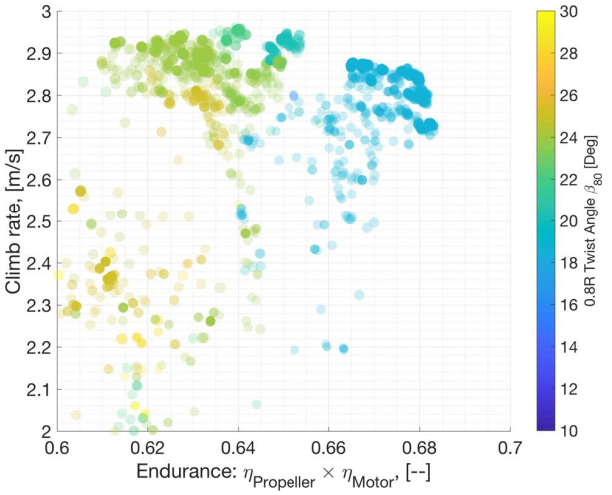

(a) Endurance

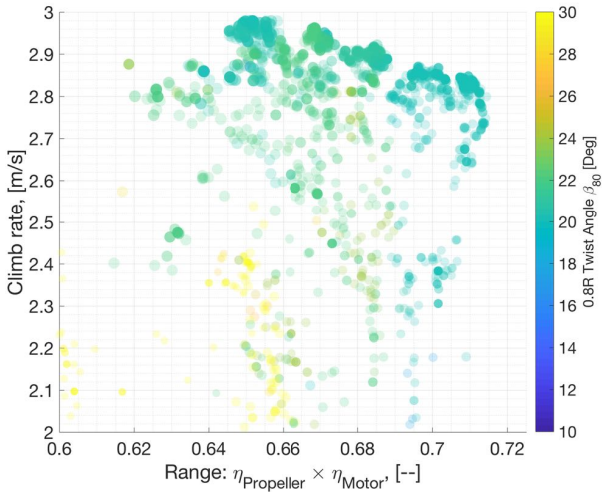

(b) Range

Fig. 12 Optimal propeller design for endurance & range vs climb-rate

It is obvious in both Figs 12(a) and 12(b) that the Pareto front is under-developed. The is due to way the current implementation of the NSGA-II algorithm deals with constraints expressed via the penalty method. More specifically, non-feasible propeller designs have their objective function values suitably penalised, but are retained as part of the Pareto front, given that they define a minimum or near-minimum in one of the objective function directions. This is a particular problem in the calculation of climb-rate, as non-feasible solutions in these cases correspond to propellers which produce extremely high climb-rates, but operate above the motor 100% throttle line. These candidate propellers are heavily penalised as a result in the current NSGA-II implementation. In future work, a more suitable treatment of constraints when using NSGA-II whereby candidate designs that are penalised are subsequently removed from the active Pareto front will be investigated. However this risks stagnation of the Pareto front if an overly-sparse front results.

4.2.3 Flight Velocity

The combination of high vehicle endurance and high maximum velocity is another desirable combination for a tactical UAS to both reduce response time and maximise time-on-station. However these design goals are almost exclusively opposed to one another for a fixed-pitch propeller, as a propeller will perform optimally when its blade sections are at their maximum lift-to-drag ratio. This occurs close to the sectional zero-lift angle, and thus any increase in maximum flight velocity will be minimal for a propeller designed for optimal operation solely during loiter and cruise as the increase in forward speed will be accompanied by a corresponding drop in thrust. To this end, Pareto-optimality between endurance and maximum flight velocity as well as range and maximum flight velocity have been investigated in this study.

In much the same way as the results for multi-objective optimisation with climb-rate showed in the previous section, the Pareto fronts in Figs 13(a) and 13(b) are noticeably under-developed. Despite this, the expected resulted

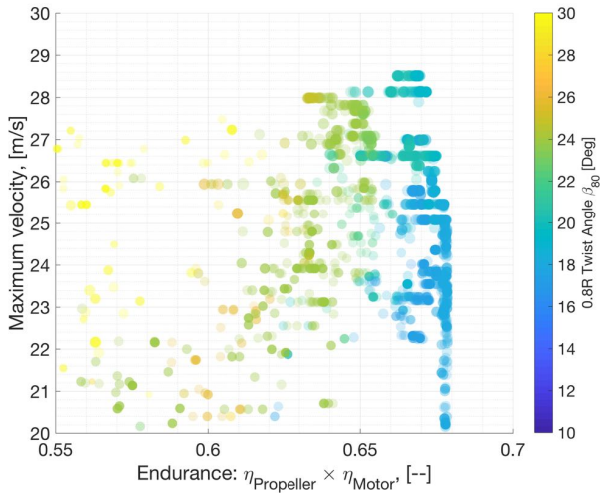

(a) Endurance

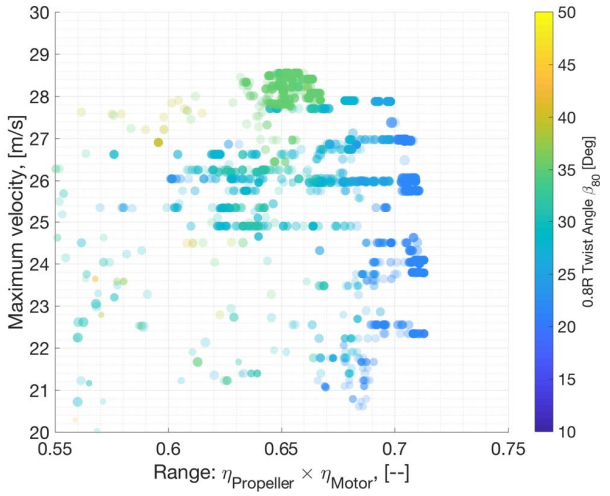

(b) Range

Fig. 13 Optimal propeller design for endurance & range vs maximum flight-velocity

is shown for the range case in Fig. 13(b) that to achieve a higher maximum flight velocity, a higher twist angle is required. Also as expected, this increase in flight velocity comes with an associated reduction of powertrain efficiency at the optimum range flight condition. In both Figs 13(a) and 13(b), the distribution of propeller diameters is seen to remain constant at all areas of the Pareto front, with differences in blade twist accounting for the difference in maximum velocity.

5 Conclusion

This paper has presented multi-objective optimisation of propellers for a small electrically-powered unmanned aerial system. A multidisciplinary optimisation method coupling an empirically corrected electric motor model, an extended blade-element-momentum theory aerodynamic model and an Euler-Bernoulli beam structural model has been used in conjunction with the NSGA-II algorithm to conduct multi-objective optimisation of a propeller-motor combination.

To allow optimisation of both the propeller and motor concurrently, a regression analysis of 1743 electric motors has been conducted. Using the resulting expressions, the characteristic parameters of a motor can be found, and its performance analysed without the need for experimental testing.

Pareto fronts showing the tradeoff between propeller and motor efficiencies have been presented for both optimal endurance and optimal range conditions for the aircraft. Additionally, Pareto optimality between aircraft endurance and range has been investigated in combination with either climb-rate or flight-velocity maximisation.

The ability of the design tool to produce optimal propellers across both single-point and multi-point optimisation has been demonstrated. In addition, the presentation of Pareto optimality between competing design goals allows the designer a quantification of the tradeoffs between different performance parameters when optimising a propeller for a small electrically-powered tactical UAS. Finally, the shortcomings of using a penalty method in combination with the NSGA-II algorithm have been identified in the form of under-developed feasible Pareto fronts.

References

[1] J. Gundlach. *Designing Unmanned Aircraft Systems: A Comprehensive Approach*. AIAA Education Series. American Institute of Aeronautics and Astronautics, 2012.

[2] D. A. Lawrence and K. Mohseni. Efficiency Analysis for Long-Duration Electric MAVs. *AIAA 2005-7090, American Institute of Aeronautics and Astronautics: Infotech @ Aerospace, Arlington, Virginia, USA*, 26 - 29 September 2005.

[3] N. Xue. *Design and Optimization of Lithium-Ion Batteries for*

Electric-Vehicle Applications. PhD thesis, University of Michigan, 2014.

[4] K. Swider-Lyons, J. MacKrell, J. Rodgers, G. Page, M. Schuette, and R. Stroman. Hydrogen fuel cell propulsion for long endurance small uavs. *AIAA Centennial of Naval Aviation Forum "100 Years of Achievement and Progress"*, September 2011.

[5] C. Chiang, C. Herwerth, M. Mirmirani, A. Ko, S. Mastuyama, S. Choi, and N. Nomnawee. Systems integration of a hybrid pem fuel cell/battery powered endurance uav. *46th AIAA Aerospace Sciences Meeting and Exhibit*, January 2008.

[6] D. Verstraete, A. Gong, D. D.-C. Lu, and J. L. Palmer. Experimental investigation of the role of the battery in the AeroStack hybrid, fuel-cell-based propulsion system for small unmanned aircraft systems. *International Journal of Hydrogen Energy*, 40(3):1598–1606, January 2015.

[7] A. Gong, J. L. Palmer, G. Brian, J. R. Harvey, and D. Verstraete. Performance of a hybrid, fuel-cell-based power system during simulated small unmanned aircraft missions. *International Journal of Hydrogen Energy*, 41(26):11418–11426, July 2016.

[8] A. Gong and D. Verstraete. Design and bench test of a fuel-cell/battery hybrid uav propulsion system using metal hydride hydrogen storage. *AIAA Propulsion and Energy Forum*, 10-12 July 2017.

[9] A. Gong and D. Verstraete. Performance of brushless dc motors and electronic speed controllers for small uav applications. *AIAA Propulsion and Energy Forum (Submitted for Publication)*, 9-11 July 2018.

[10] J. A. Baranski, M. H. Fernelius, J. L. Hoke, C. W. Wilson, and P. J. Litke. Characterization of Propeller Performance and Engine Mission Matching for Small Remotely Piloted Aircraft. *AIAA 2011-6058, 47th AIAA/ASME/SAE/ASEE Joint Propulsion Conference & Exhibit, San Diego, California, USA*, 31 July - 3 August 2011.

[11] O. Gur and A. Rosen. Optimization of propeller based propulsion system. *AIAA Journal of Aircraft*, 46(1):95–106, January-February 2009.

[12] R. MacNeill and D. Verstraete. Blade element momentym theory extended to model low reynolds number propeller performance. *The Aeronautical Journal*, 121(1240):835–857, June 2017.

[13] J. Sobieszczanski-Sobieski and R. T. Haftka. Multidisciplinary aerospace design optimization: survey of recent developments. *Structural Optimization*, 14(1):1–23, 1997.

[14] Ohad Gur and Aviv Rosen. Design of a quiet propeller for an electric mini unmanned air vehicle. *AIAA Journal of Propulsion and Power*, 25(3):717–728, May-June 2009.

[15] O. Gur and A. Rosen. Optimizing electric propulsion systems for unmanned aerial vehicles. *AIAA Journal of Aircraft*, 46(4):1340–1353, July-August 2009.

[16] P. Pounds and R. Mahony. Small-scale aeroelastic rotor simulation, design and fabrication. *Proceedings of the 2005 Australasian Conference on Robotics and Automation*, 2005.

[17] J. Sodja, D. Stadler, and T. Kosel. Computational fluid dynamics analysis of an optimized load-distribution propeller. *AIAA Journal of Aircraft, Engineering Notes*, 49(3):955–961, May-June 2012.

[18] J. Sodja, R. Drazumeric, and T. Kosel. Design of flexible propellers with optimized load-distribution characteristics. *AIAA Journal of Aircraft*, 51(1):117–128, January-February 2014.

[19] R. MacNeill and D. Verstraete. Optimal propellers for a small hybrid electric fuel-cell uas. *AIAA-IEEE Electric Aircraft Technologies Symposium*, July 2018.

[20] Briand David Rutkay. A process for the design and manufacture of propellers for small unmanned aerial vehicles. Master's thesis, Carleton University, 2014.

[21] D. L. Wall. Optimum Propeller Design for Electric UAVs. Master's thesis, Auburn University, Auburn, Alabama, USA, August 2012.

[22] R. R. Glassock. Design, modelling and measurement of hybrid powerplant for unmanned aerial vehicles (UAVs). Master's thesis, School of Electrical Engineering and Computer Science, Queensland University of Technology, 2012.

[23] T. Rotramel. Optimization of hybrid-electric propulsion systems for small remotely-piloted aircraft. Master's thesis, Air Force Institute of Technology, March 2011.

[24] N. Nguyen, J. Lee, M. Tyan, and D. Lee. Possibility-based multidisciplinary optimisation for electric-powered unmanned aerial vehicle design. *The Aeronautical Journal*, 119(1221):1397–1414, November 2015.

[25] M. Bronz, J-M. Moschetta, and G. Hattenberger. Multi-point optimisation of a propulsion set as applied to a multi-tasking mav. *IMAV 2012, International Micro Aerial Vehicle Conference and Competition, Braunschweig, Germany*, July 2012.

[26] K. Deb, A. Pratap, and T. Meyarivan. A fast and elitist multiobjective genetic algorithm: Nsga-ii. *IEEE Transactions on Evolutionary Computation*, 6(2):182–197, April 2002.

[27] Mark Drela. First-order dc electric motor model. Technical report, Massachusetts Institute of Technology, February 2007.

[28] D. Verstraete, J. L. Palmer, and M. Hornung. Preliminary sizing correlations for fixed-wing unmanned aerial vehicle characteristics. *AIAA Journal of Aircraft*, 55(2):715–728, 2017.

[29] Duane Hanselman. *Brushless permanent magnet motor design*. Cranston, R.I. : The Writers' Collective, second edition, 2003.

[30] Agnieszka Makowska. Electric propulsion components with high power densities for aviation. In *Proceedings of the Symposium E2-Fliegen*, Stuttgart, Germany, 2015.

[31] *Koenigsegg Regera Specifications*. Koenigsegg, Last Accessed: December 2016. http://koenigsegg.com/regera/.

[32] R.D. Lorenz. Flight power scaling of airplanes, airships, and helicopters: Application to planetary exploration. *Journal of Aircraft*, 38(2):208–214, 2001.

[33] T. Liu. Comparative scaling of flapping- and fixed-wing flyers. *AIAA Journal*, 44(1):24–33, 2006.

[34] T. Liu, A. Oyama, and K. Fujii. Scaling analysis of propeller-driven aircraft for mars exploration. *Journal of Aircraft*, 50(5):1593–16–4, 2013. doi: 10.2514/1.C032086.

[35] O. Gur and A. Rosen. Propeller Performance at Low Advance Ratio. *AIAA Journal of Aircraft*, 42(2):435–441, March-April 2005.

[36] R. MacNeill, D. Verstraete, and A. Gong. Optimisation of Propellers for UAV Powertrains. *AIAA Propulsion and Energy Forum*, 2017.

[37] T. R. Chandrupatla and A. D. Belegundu. *Introduction to Finite Elements in Engineering*. Prentice Hall, 3 edition, 2002.

[38] O. A. Bauchau and J. I. Craig. *Structural Analysis With Applications to Aerospace Structures*. Solid Mechanics and Its Applications. Springer, 2009.

[39] S. Boyd and L. Vandenberghe. *Convex Optimization*. Cambridge University Press, 2004.

[40] A. Forrester, A. Sobester, and A. Keane. *Engineering Design via Surrogate Modelling*. John Wiley and Sons, 2008.

[41] B. Tang. Orthogonal Array-Based Latin Hypercubes. *Journal of the American Statistical Association*, 88(424):1392–1397, December 1993.

[42] R. C. Hibbeler. *Mechanics of Materials*. Prentice Hall, 8 edition, 2011.

6 Contact Author Email Address

rens.macneill@sydney.edu.au

Copyright Statement